Analysis of enhanced second-harmonic generation in periodic nanostructures using modified rigorous coupled-wave analysis in the undepleted-pump approximation

Wataru Nakagawa, Rong-Chung Tyan, and Yeshaiahu Fainman

Department of Electrical and Computer Engineering, University of California, San Diego, 9500 Gilman Drive, La Jolla, California 92093-0407

Received December 21, 2001; revised manuscript received April 10, 2002; accepted April 16, 2002

We present an extension of the rigorous coupled-wave analysis technique to analyze second-harmonic generation (SHG) in periodic optical nanostructures in the undepleted-pump approximation. We apply this method to analyze SHG in two example nanostructures for which we predict enhanced nonlinearity due to transverse near-field localization of the fundamental optical field in the nonlinear material. First, we examine a periodic nanostructure that yields up to twice the transmitted SHG intensity output compared with the bulk nonlinear material but only for small nanostructure depths because of mismatch of the fundamental and second-harmonic mode phase velocities. Second, we develop and analyze a modified nanostructure and find that this nanostructure concurrently achieves transverse localization and phase matching for SHG. In principle, this permits an arbitrary coherent interaction length, and for several specific nanostructure depths we predict a transmitted SHG intensity output more than two orders of magnitude greater than that of the bulk material.

OCIS codes: 150.1970, 230.4320, 190.4420, 190.2620, 000.4430.

1. INTRODUCTION

Recent developments in microfabrication techniques and nanoscale photonic technologies suggest that integrated optical or photonic systems based on these technologies may be realized in the near future. In particular, any high-level integrated photonic system will almost certainly require the inclusion of nonlinear optical processes (e.g., to achieve wavelength conversion, switching, signal amplification, or system reconfigurability). However, most standard nonlinear optical materials are not readily compatible with standard microfabrication materials and techniques. Fortunately, nanostructured material and device technologies, including artificial dielectric nanostructures,[1,2] form-birefringent nanostructures,[3,4] and photonic crystals,[5–7] may provide a means to overcome these incompatibilities. Since optical nanostructures permit the engineering of their effective optical properties, they facilitate realization of the desired linear and nonlinear optical functionalities with use of compatible materials and processes.

Photonic nanostructures not only facilitate the integration of various optical devices but may also permit improvement or enhancement of their optical functionality. We have previously investigated transverse localization of the optical field inside a periodic nanostructure and its potential application to the enhancement of nonlinear optical phenomena such as second-harmonic generation (SHG).[8] We predicted that the electromagnetic fields inside the nanostructure would experience strong transverse localization, significantly elevating the field amplitude in the nonlinear material and thus enhancing the SHG output. Similar enhancement of nonlinear optical effects though near-field localization in a variety of subwavelength optical structures has been predicted and observed by a number of investigators.[9–13] Further nonlinearity enhancement may be realized by achieving phase matching between the fundamental and second-harmonic (SH) fields in a nanostructure.[14–19] To achieve the largest SHG output, we investigate a nanostructure that employs both enhancement mechanisms: near-field localization and improved phase matching.

In order to accurately design and analyze nonlinear optical processes in subwavelength nanostructures, it is necessary to develop appropriate rigorous modeling tools. The rigorous coupled-wave analysis[20] (RCWA) technique is a well-established tool for analyzing linear electromagnetic wave interactions with subwavelength periodic structures in both the near- and the far-field regimes. In this paper we extend the RCWA method by using a perturbational expansion of the nonlinear polarization term of Maxwell's equations to analyze the nonlinear SHG process in the undepleted-pump approximation. The resulting electromagnetic analysis tool permits an accurate investigation of the SHG enhancement in periodic optical nanostructures. In Section 2 we describe the extension of RCWA to model SHG in the undepleted-pump approximation. In Section 3 we apply this tool to study the SHG enhancement resulting from two nanostructures: the original design of Ref. 8 and a modified structure optimized for phase matching. We present a summary and conclusions in Section 4.

2. ELECTROMAGNETIC ANALYSIS METHOD

A. Frequency-Separable Formulation of Maxwell's Equations

To analyze SHG in the undepleted-pump approximation by using RCWA, we assume that electromagnetic fields exist only at the fundamental and second-harmonic frequencies, yielding total fields

$$\vec{E}(\vec{r}, t) = \vec{E}_\omega(\vec{r})\exp(j\omega t) + \vec{E}_{2\omega}(\vec{r})\exp(j2\omega t), \quad (1)$$

$$\vec{H}(\vec{r}, t) = \vec{H}_\omega(\vec{r})\exp(j\omega t) + \vec{H}_{2\omega}(\vec{r})\exp(j2\omega t), \quad (2)$$

where $\vec{E}_\omega(\vec{r})$ and $\vec{E}_{2\omega}(\vec{r})$ are time-harmonic representations of the electric fields at the fundamental and second-harmonic frequencies, respectively, and $\vec{H}_\omega(\vec{r})$ and $\vec{H}_{2\omega}(\vec{r})$ are time-harmonic representations of the magnetic fields at the fundamental and second-harmonic frequencies, respectively. We assume $\mu = \mu_0$ for simplicity. Since we wish to investigate nonlinear phenomena in nanostructures, we must allow the electric displacement to include both linear and nonlinear effects:

$$\vec{D}(\vec{r}, t) = \epsilon\vec{E}(\vec{r}, t) + \vec{P}_{\mathrm{NL}}(\vec{r}, t). \quad (3)$$

However, for simplicity we assume that the nonlinear polarization term contains only the sum-frequency generation of the second harmonic from the fundamental frequency

$$\vec{P}_{\mathrm{NL}}(\vec{r}, t) = \frac{\chi^{(2)}}{2}\vec{E}_\omega(\vec{r})\exp(j\omega t)\vec{E}_\omega(\vec{r})\exp(j\omega t) \quad (4)$$

and ignore all other $\chi^{(2)}$ phenomena such as difference-frequency generation, optical rectification, or cascaded nonlinear effects, as is consistent with the undepleted-pump approximation. Substituting into Maxwell's equations, we find that

$$\nabla \times [\vec{E}_\omega(\vec{r})\exp(j\omega t) + \vec{E}_{2\omega}(\vec{r})\exp(j2\omega t)] = -\mu\frac{\partial}{\partial t}[\vec{H}_\omega(\vec{r})\exp(j\omega t) + \vec{H}_{2\omega}(\vec{r})\exp(j2\omega t)] \quad (5)$$

$$\nabla \times [\vec{H}_\omega(\vec{r})\exp(j\omega t) + \vec{H}_{2\omega}(\vec{r})\exp(j2\omega t)] = \frac{\partial}{\partial t}[\epsilon_\omega\vec{E}_\omega(\vec{r})\exp(j\omega t) + \epsilon_{2\omega}\vec{E}_{2\omega}(\vec{r})\exp(j2\omega t) + \vec{P}_{\mathrm{NL}}(\vec{r}, t)], \quad (6)$$

where ϵ_ω and $\epsilon_{2\omega}$ are the dielectric constants of the material at the fundamental and second-harmonic frequencies, respectively, which in general will be different owing to material dispersion. Equations (5) and (6) can be decoupled into two sets of coupled differential equations at the fundamental and second-harmonic frequencies. At the fundamental frequency we obtain the standard homogeneous form of Maxwell's equations:

$$\nabla \times \vec{E}_\omega(\vec{r}) = -j\omega\mu\vec{H}_\omega(\vec{r}) \quad (7)$$

$$\nabla \times \vec{H}_\omega(\vec{r}) = j\omega\epsilon_\omega\vec{E}_\omega(\vec{r}). \quad (8)$$

The propagation of the fundamental-frequency field through the structure is determined by using the standard RCWA approach and is summarized in Appendix A to introduce the notation used in the remainder of this section as well as to provide a self-contained description of the SHG RCWA method. At the second-harmonic frequency, however, we obtain an inhomogeneous system of equations that are due to the nonlinear polarization term:

$$\nabla \times \vec{E}_{2\omega}(\vec{r}) = -j2\omega\mu\vec{H}_{2\omega}(\vec{r}), \quad (9)$$

$$\nabla \times \vec{H}_{2\omega}(\vec{r}) = j2\omega\epsilon_{2\omega}\vec{E}_{2\omega}(\vec{r}) + j\omega\chi^{(2)}\vec{E}_\omega(\vec{r})\vec{E}_\omega(\vec{r}). \quad (10)$$

This inhomogeneous system of equations can be treated with standard techniques and is described in detail in the following sections.

It is important to note that useful information about the eigenmodes of the periodic structure can be readily obtained from this formulation of the RCWA method. The electromagnetic fields inside the structure are represented as a superposition of the eigenmodes, as shown in Eq. (A8). Each column of the eigenvector matrix $\mathbf{W}_\omega$ describes one of the eigenmodes of the grating, with the respective eigenvalue corresponding to the propagation constant of that mode and the coefficient corresponding to the complex amplitude of that mode. This information can be used to identify the energy-carrying modes of the grating structure and to compare the propagation constant and the transverse profile of each of those modes.

B. Nonlinear Polarization

In the standard RCWA formulation, owing to the periodic nature of the grating a space-harmonic expansion of the dielectric constant function of the grating is performed. In a similar fashion, we can also expand the nonlinear coefficient $\chi^{(2)}$ using a space harmonic expansion:

$$\chi^{(2)}(x) = \sum_k \tilde{\chi}_k \exp(jkK_g x). \quad (11)$$

Using the expansions shown in Eqs. (A2) and (11), we can write the undepleted-pump nonlinear polarization term as

$$\vec{P}_{\mathrm{NL}}(\vec{r}) \approx \sum_i \sum_h \sum_k \tilde{\chi}_k\vec{S}_{\omega,i}\vec{S}_{\omega,h} \times \exp\{-j[(\vec{\sigma}_{\omega,i} + \vec{\sigma}_{\omega,h})\cdot\vec{r} - kK_g x]\}. \quad (12)$$

Expanding the argument of the exponential function, we find

$$(\vec{\sigma}_{\omega,i} + \vec{\sigma}_{\omega,h})\cdot\vec{r} - kK_g x = [2k_{\mathrm{inc},\omega,x} - (i + h + k)K_g]x + 2k_{\mathrm{inc},\omega,y}y. \quad (13)$$

Since the fundamental field and the nonlinear coefficient are all represented by harmonic expansions based on the period of the grating, it is possible to write the nonlinear polarization term as a single space-harmonic expansion,

$$P_{\mathrm{NL},v}(\vec{r}, t) = \sum_i P_{i,v}(z)\exp\{-j[(2k_{\mathrm{inc},x} - iK_g)x + 2k_{\mathrm{inc},y}y]\}, \quad (14)$$

where

$$
\begin{aligned}
P_{i,v}(z) = \sum_h \sum_k \{ & \tilde{\chi}_{vxx,i-h-k} S_{\omega,h,x} S_{\omega,k,x} \\
& + \tilde{\chi}_{vxy,i-h-k} S_{\omega,h,x} S_{\omega,k,y} \\
& + \tilde{\chi}_{vxz,i-h-k} S_{\omega,h,x} S_{\omega,k,z} \\
& + \tilde{\chi}_{vyx,i-h-k} S_{\omega,h,y} S_{\omega,k,x} \\
& + \tilde{\chi}_{vyy,i-h-k} S_{\omega,h,y} S_{\omega,k,y} \\
& + \tilde{\chi}_{vyz,i-h-k} S_{\omega,h,y} S_{\omega,k,z} \\
& + \tilde{\chi}_{vzx,i-h-k} S_{\omega,h,z} S_{\omega,k,x} \\
& + \tilde{\chi}_{vzy,i-h-k} S_{\omega,k,z} S_{\omega,k,y} \\
& + \tilde{\chi}_{vzz,i-h-k} S_{\omega,k,z} S_{\omega,k,z} \}
\end{aligned} \tag{15}
$$

and $v \in \{x, y, z\}$.

In analyzing the fields at the second-harmonic frequency, we perform a space-harmonic expansion of the fields similar to that of Eqs. (A2) and (A3):

$$
\begin{aligned}
\vec{E}_{2\omega}(\vec{r}) = \sum_i & \{ S_{2\omega,i,x}(z)\hat{x} + S_{2\omega,i,y}(z)\hat{y} \\
& + S_{2\omega,i,z}(z)\hat{z} \} \exp(-j\vec{\sigma}_{2\omega,i} \cdot \vec{r})
\end{aligned} \tag{16}
$$

$$
\begin{aligned}
\vec{H}_{2\omega}(\vec{r}) = & \sqrt{\frac{\epsilon_0}{\mu_0}} \sum_i \{ U_{2\omega,i,x}(z)\hat{x} + U_{2\omega,i,y}(z)\hat{y} \\
& + U_{2\omega,i,z}(z)\hat{z} \} \exp(-j\vec{\sigma}_{2\omega,i} \cdot \vec{r})
\end{aligned} \tag{17}
$$

To find the transverse wave vector, we consider that the second-harmonic field is generated by the fundamental field, and thus the transverse components of the second harmonic wave vector must be directly related to those at the fundamental frequency:

$$
\vec{\sigma}_{2\omega,i} = (2k_{\mathrm{inc},x} - iK_g)\hat{x} + 2k_{\mathrm{inc},y}\hat{y}. \tag{18}
$$

To match the range of the space-harmonic expansion, the second-harmonic field expansion must have $2p - 1 = 4a + 1$ components indexed by $i \in \{-2a, \ldots, -1, 0, 1, \ldots, 2a\}$.

C. Solution of the Second-Harmonic-Frequency Fields

Using the inhomogeneous equations for the fields at the second-harmonic frequency, and inserting the space-harmonic expansions for the electric and magnetic fields shown in Eqs. (16) and (17), respectively, as well as the expansion for the nonlinear polarization shown in Eq. (15), we obtain a coupled system of equations in matrix form:

$$
\begin{aligned}
\frac{\partial}{\partial z} \begin{pmatrix} \vec{S}_{2\omega,x}(z) \\ \vec{S}_{2\omega,y}(z) \\ \vec{U}_{2\omega,x}(z) \\ \vec{U}_{2\omega,y}(z) \end{pmatrix} = & \mathbf{A}_{2\omega} \begin{pmatrix} \vec{S}_{2\omega,x}(z) \\ \vec{S}_{2\omega,y}(z) \\ \vec{U}_{2\omega,x}(z) \\ \vec{U}_{2\omega,y}(z) \end{pmatrix} \\
& + \begin{pmatrix} \bar{k}_{2\omega,x} \bar{\epsilon}^{-1}_{2\omega,zz} \vec{P}_z(z) \\ \bar{k}_{2\omega,y} \bar{\epsilon}^{-1}_{2\omega,zz} \vec{P}_z(z) \\ \vec{P}_y(z) - \bar{\epsilon}_{2\omega,yz} \bar{\epsilon}^{-1}_{2\omega,zz} \vec{P}_z(z) \\ -\vec{P}_x(z) + \bar{\epsilon}_{2\omega,xz} \bar{\epsilon}^{-1}_{2\omega,zz} \vec{P}_z(z) \end{pmatrix},
\end{aligned} \tag{19}
$$

where the matrix $\mathbf{A}_{2\omega}$ represents the coupling between modes that are due to the properties of the grating and Maxwell's equations and is essentially the same as in the homogeneous fundamental-frequency solution. This inhomogeneous system of equations can then be solved by using standard techniques. Defining

$$
\begin{pmatrix} \vec{S}_{2\omega,x}(z) \\ \vec{S}_{2\omega,y}(z) \\ \vec{U}_{2\omega,x}(z) \\ \vec{U}_{2\omega,y}(z) \end{pmatrix} = \mathbf{W}_{2\omega} \vec{Q}(z), \tag{20}
$$

where $\mathbf{W}_{2\omega}$ is the eigenvector matrix obtained from matrix $\mathbf{A}_{2\omega}$ [equivalent to matrix $\mathbf{W}_\omega$ shown in Eq. (A8) but for the second-harmonic frequency), we can write the system of partial differential equations in Eq. (19) as

$$
\frac{\partial}{\partial z} \vec{Q}(z) = \mathbf{W}^{-1}_{2\omega} \mathbf{A}_{2\omega} \mathbf{W}_{2\omega} \vec{Q}(z) + \mathbf{W}^{-1}_{2\omega} \vec{Y}(z), \tag{21}
$$

where

$$
\vec{Y}(z) = \begin{pmatrix} \bar{k}_{2\omega,x} \bar{\epsilon}^{-1}_{2\omega,zz} \vec{P}_z(z) \\ \bar{k}_{2\omega,y} \bar{\epsilon}^{-1}_{2\omega,zz} \vec{P}_z(z) \\ \vec{P}_y(z) - \bar{\epsilon}_{2\omega,yz} \bar{\epsilon}^{-1}_{2\omega,zz} \vec{P}_z(z) \\ -\vec{P}_x(z) + \bar{\epsilon}_{2\omega,xz} \bar{\epsilon}^{-1}_{2\omega,zz} \vec{P}_z(z) \end{pmatrix}. \tag{22}
$$

The partial differential equation shown in Eq. (21) consists of a homogeneous and an inhomogeneous part, so we explicitly separate the homogeneous and the inhomogeneous parts of the solution:

$$
\vec{Q}(z) = \vec{Q}^{(\mathrm{h})}(z) + \vec{Q}^{(\mathrm{ih})}(z). \tag{23}
$$

The homogeneous part of the solution is the same as in the fundamental-frequency case:

$$
\vec{Q}^{(\mathrm{h})}_i(z) = c_{2\omega,i} \exp[\lambda_{2\omega,i}(z - z_{0,i})], \tag{24}
$$

where $c_{2\omega,i}$ is the amplitude coefficient of the ith eigenmode to the determined by the boundary conditions, $\lambda_{2\omega,i}$ is the eigenvalue corresponding to the ith eigenmode, and $z_{0,i}$ is defined by

$$
z_{0,i} = \begin{cases} d, & 0 \leq i < 2p \\ 0, & 2p \leq i < 4p \end{cases}. \tag{25}
$$

The renormalization shown in Eq. (25) is performed to enhance numerical stability (see Ref. 21 for a more detailed explanation). The inhomogeneous part of the solution produces the inhomogeneous term in the partial differential equation of Eq. (21) and is given by

$$
\vec{Q}^{(\mathrm{ih})}_i(z) = \begin{cases} \exp(\lambda_{2\omega,i} z) \displaystyle\int_d^z \exp(-\lambda_{2\omega,i} z') \\ \quad \times \displaystyle\sum_j \mathbf{W}^{-1}_{2\omega,ij} Y_j(z') \mathrm{d}z', & 0 \leq i < 2p, \\ \exp(\lambda_{2\omega,i} z) \displaystyle\int_0^z \exp(-\lambda_{2\omega,i} z') \\ \quad \times \displaystyle\sum_j \mathbf{W}^{-1}_{2\omega,ij} Y_j(z') \mathrm{d}z', & 2p \leq i < 4p, \end{cases} \tag{26}
$$

with use of a renormalization similar to that shown in Eq. (25).

Including the inhomogeneous part of the solution with the same renormalization as shown in Eq. (25), we find that the field mode amplitude coefficients at the front interface of the grating structure are given by

$$\vec{Q}_i(0) = \begin{cases} c^-_{2\omega,i}\exp(-\lambda_{2\omega,i}d) \\ \quad - \int_0^d \exp(-\lambda_{2\omega,i}z')\sum_j \mathbf{W}^{-1}_{2\omega,ij}Y_j(z')\mathrm{d}z', \\ \qquad\qquad 0 \leqslant i < 2p, \\ c^+_{2\omega,i}, \qquad\qquad 2p \leqslant i < 4p, \end{cases} \tag{27}$$

and at the back interface of the grating structure ($z = d$) we find that

$$\vec{Q}_i(d) = \begin{cases} c^-_{2\omega,i}, \qquad\qquad 0 \leqslant i < 2p, \\ c^+_{2\omega,i}\exp(\lambda_{2\omega,i}d) + \exp(\lambda_{2\omega,i}d) \\ \quad \times \int_0^d \exp(-\lambda_{2\omega,i}z')\sum_j \mathbf{W}^{-1}_{2\omega,ij}Y_j(z')\mathrm{d}z', \\ \qquad\qquad 2p \leqslant i < 4p. \end{cases} \tag{28}$$

Substituting Eqs. (27) and (28) into Eq. (20), we can obtain the space-harmonic expansion coefficients of the fields at the second-harmonic frequency at the front and back interfaces of the nonlinear grating layer.

D. Boundary Condition Matching

To obtain the complete solution of the fields inside the nanostructure, it is necessary to determine the unknown coefficients $\{c_{2\omega}\}$ by matching the tangential components of the fields at each interface. The fields in the incident and transmitted half-spaces on either side of the grating can be represented by a set of plane waves with transverse wave vectors matched to the space-harmonic modes inside the grating. Thus there are $p = 2a + 1$ plane waves in each half-space, with complex amplitude coefficients collected into vectors $\vec{r}$ and $\vec{t}$ in the incident and transmitted half-spaces, respectively. The space-harmonic representation of the transmitted fields at the interface ($z = d^+$) can be written as

$$\begin{pmatrix} \vec{S}_{2\omega,x}(d^+) \\ \vec{S}_{2\omega,y}(d^+) \\ \vec{U}_{2\omega,x}(d^+) \\ \vec{U}_{2\omega,y}(d^+) \end{pmatrix} = \begin{bmatrix} \mathbf{0} & \mathbf{I} \\ \mathbf{0} & \mathbf{H} \end{bmatrix} \begin{pmatrix} \vec{r} \\ \vec{t} \end{pmatrix}, \tag{29}$$

where $\mathbf{I}$ is the identity matrix and matrix $\mathbf{H}$ yields the magnetic field amplitude coefficients from the electric-field amplitude coefficients of the free-space modes in the half-spaces on either side of the structure. These relations can be found in a straightforward way by using Eq. (7), and an explicit definition of the elements of matrix $\mathbf{H}$ can be found in Eq. (22) or Eq. (26) of Ref. 20. Similarly, the space-harmonic representation of the fields at the incident boundary ($z = 0^-$) is given by

$$\begin{pmatrix} \vec{S}_{2\omega,x}(0^-) \\ \vec{S}_{2\omega,y}(0^-) \\ \vec{U}_{2\omega,x}(0^-) \\ \vec{U}_{2\omega,y}(0^-) \end{pmatrix} = \begin{bmatrix} \mathbf{I} & \mathbf{0} \\ \mathbf{H} & \mathbf{0} \end{bmatrix} \begin{pmatrix} \vec{r} \\ \vec{t} \end{pmatrix} + \begin{bmatrix} \mathbf{I} & \mathbf{0} \\ \mathbf{H} & \mathbf{0} \end{bmatrix} \begin{pmatrix} \vec{b} \\ 0 \end{pmatrix}, \tag{30}$$

where the vector $\vec{b}$ represents the incident field. For the fundamental-frequency waves, the vector $\vec{b}$ is unity for the elements corresponding to zeroth-order electric and magnetic fields and zero otherwise [see Eqs. (21) and (22) of Ref. 20]. In contrast, for the second-harmonic waves, the field is assumed to be generated inside the nonlinear material, and the externally incident field is uniformly zero.

Owing to the orthogonality of the space-harmonic basis, at each interface every transverse space-harmonic component must independently satisfy the boundary conditions. By combining Eqs. (20), (27), and (30) for the fields at the incident boundary, we obtain the expression

$$\begin{bmatrix} \mathbf{I} & \mathbf{0} \\ \mathbf{H} & \mathbf{0} \end{bmatrix} \begin{pmatrix} \vec{r} \\ \vec{t} \end{pmatrix} + \begin{pmatrix} \mathbf{I}\vec{b} \\ \mathbf{H}\vec{b} \end{pmatrix} = \begin{bmatrix} \mathbf{W}^{00}_{2\omega}[\exp(-\lambda_{2\omega}d)] & \mathbf{W}^{01}_{2\omega} \\ \mathbf{W}^{10}_{2\omega}[\exp(-\lambda_{2\omega}d)] & \mathbf{W}^{11}_{2\omega} \end{bmatrix} \begin{pmatrix} \vec{c}^-_{2\omega,i} \\ \vec{c}^+_{2\omega,i} \end{pmatrix} + \begin{bmatrix} \mathbf{W}^{00}_{2\omega} & \mathbf{W}^{01}_{2\omega} \\ \mathbf{W}^{10}_{2\omega} & \mathbf{W}^{11}_{2\omega} \end{bmatrix} \begin{pmatrix} -\vec{Q}^{(\mathrm{ih}),-}(0) \\ 0 \end{pmatrix}, \tag{31}$$

where $\vec{Q}^{(\mathrm{ih}),-}(0)$ indicates only the top half ($0 \leqslant i < 2p$) of the vector $\vec{Q}^{(\mathrm{ih})}(0)$, and the expansion

$$\mathbf{W}_{2\omega} = \begin{bmatrix} \mathbf{W}^{00}_{2\omega} & \mathbf{W}^{01}_{2\omega} \\ \mathbf{W}^{10}_{2\omega} & \mathbf{W}^{11}_{2\omega} \end{bmatrix}$$

has been applied. Similarly, by combining Eqs. (20), (28), and (29) for the fields at the transmitted boundary, we obtain the expression

$$\begin{bmatrix} \mathbf{0} & \mathbf{I} \\ \mathbf{0} & \mathbf{H} \end{bmatrix} \begin{pmatrix} \vec{r} \\ \vec{t} \end{pmatrix} = \begin{bmatrix} \mathbf{W}^{00}_{2\omega} & \mathbf{W}^{01}_{2\omega}[\exp(\lambda_{2\omega}d)] \\ \mathbf{W}^{00}_{2\omega} & \mathbf{W}^{11}_{2\omega}[\exp(\lambda_{2\omega}d)] \end{bmatrix} \begin{pmatrix} \vec{c}^-_{2\omega} \\ \vec{c}^+_{2\omega} \end{pmatrix} + \begin{bmatrix} \mathbf{W}^{00}_{2\omega} & \mathbf{W}^{01}_{2\omega} \\ \mathbf{W}^{10}_{2\omega} & \mathbf{W}^{11}_{2\omega} \end{bmatrix} \begin{pmatrix} 0 \\ \vec{Q}^{(\mathrm{ih}),+}(d) \end{pmatrix}, \tag{32}$$

where $\vec{Q}^{(\mathrm{ih}),+}(d)$ indicates only the bottom half ($2p \leqslant i < 4p$) of the vector $\vec{Q}^{(\mathrm{ih})}(d)$.

Owing to numerical stability issues, Eqs. (31) and (32) cannot be solved by substitution.[21] Instead, we combine them into a single system of equations:

$$\begin{bmatrix} \mathbf{W}^{00}_{2\omega}[\exp(-\lambda_{2\omega}d)] & \mathbf{W}^{01}_{2\omega} & -\mathbf{I} & \mathbf{0} \\ \mathbf{W}^{10}_{2\omega}[\exp(-\lambda_{2\omega}d)] & \mathbf{W}^{11}_{2\omega} & -\mathbf{H} & \mathbf{0} \\ \mathbf{W}^{00}_{2\omega} & \mathbf{W}^{01}_{2\omega}[\exp(\lambda_{2\omega}d)] & \mathbf{0} & -\mathbf{I} \\ \mathbf{W}^{10}_{2\omega} & \mathbf{W}^{11}_{2\omega}[\exp(\lambda_{2\omega}d)] & \mathbf{0} & -\mathbf{H} \end{bmatrix} \times \begin{pmatrix} \vec{c}^-_{2\omega} \\ \vec{c}^+_{2\omega} \\ \vec{r} \\ \vec{t} \end{pmatrix} = \begin{pmatrix} \mathbf{W}^{00}_{2\omega}\vec{Q}^{(\mathrm{ih}),-}(0) + \mathbf{I}\vec{b} \\ \mathbf{W}^{10}_{2\omega}\vec{Q}^{(\mathrm{ih}),-}(0) + \mathbf{H}\vec{b} \\ -\mathbf{W}^{01}_{2\omega}\vec{Q}^{(\mathrm{ih}),+}(d) \\ -\mathbf{W}^{11}_{2\omega}\vec{Q}^{(\mathrm{ih}),+}(d) \end{pmatrix}. \tag{33}$$

Solution of Eq. (33) yields the complex amplitude coefficients $\vec{r}$, $\vec{c}_{2\omega}$, and $\vec{t}$, which respectively describe the re-

flected, internal, and transmitted fields of the grating at the second-harmonic frequency. Thus this technique permits the analysis of second-order nonlinear optical phenomena in periodic nanostructures in the undepleted-pump approximation.

3. NANOSTRUCTURE DESIGN FOR ENHANCED SECOND-HARMONIC GENERATION

A. Transverse Near-Field Localization

In a previous paper[8] we described the transverse localization of the fundamental frequency field in a periodic subwavelength nanostructure and performed an approximate analysis of the enhancement of the SHG output that is due to this localization. This approximate analysis was based solely on transverse effects, and thus it did not take into account the mismatch in the phase velocities of the fundamental and second-harmonic fields or the effects of the finite length of the nanostructure. For a more accurate analysis, we apply the extended RCWA method described above to investigate a similar structure, but for a very small grating thickness and replacing ultrashort-pulse illumination with a monochromatic field. The nanostructure is a subwavelength square grating (see Fig. 1) of period $\Lambda = 0.65\lambda$, fill factor $F = 0.09$, and depth varying from $d = 0.005\lambda$ to $d = 5.0\lambda$ in units of the fundamental wavelength in vacuum. The refractive index of the material is taken to be $n_\omega = 3.346$ at the fundamental frequency and $n_{2\omega} = 3.539$ at the second-harmonic frequency, corresponding to the material properties of GaAs at 1.907 μm and 0.954 μm, respectively. These particular values were selected to ensure that the absorption coefficient of GaAs is negligible for both the fundamental and the second-harmonic wavelengths. The nonlinear coefficient is taken to be 0.001 in inverse units of the field amplitude, corresponding to the second-order nonlinear coefficient of GaAs ($\chi^{(2)} = 240$ pm/V from Ref. 15) with an applied field amplitude of 4.17×10^6 V/m. The fundamental and second-harmonic fields are both assumed to be polarized in the $\hat{y}$ direction, as shown in Fig. 1. A nanostructure of this type would be fabricated most easily either by deep etching into a substrate or a multilayer growth; the resulting structure would differ from that shown in Fig. 1 because of the presence of the substrate and the finite extent of the structure in the transverse direction. Although it is possible to perform the analysis for a structure that incorporates these characteristics, the interpretation of the results would be significantly more complicated and therefore less clear. Thus we analyze the simple nanostructure shown in Fig. 1—which is assumed to be infinitely periodic in the $\hat{x}$ direction, infinite and uniform in the $\hat{y}$ direction, finite and uniform in the $\hat{z}$ direction, surrounded by vacuum on both sides, and not explicitly including the substrate—in order to investigate and present in a straightforward manner the fundamental characteristics of the optical field interaction with the nanostructure.

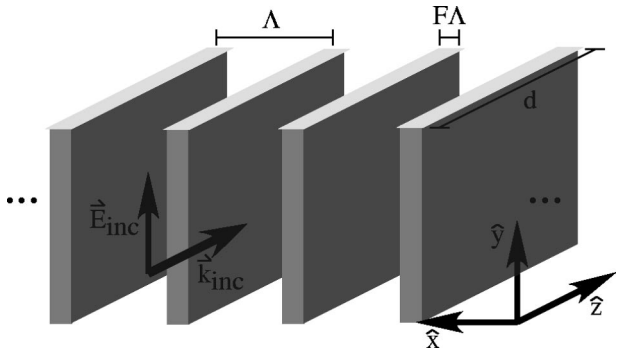

Fig. 1. Schematic diagram of the transverse field localization nanostructure for SHG enhancement. The nanostructure is a subwavelength periodic square grating with period $\Lambda = 0.65\lambda$, fill factor $F = 0.09$, index of refraction $n_\omega = 3.346$ at the fundamental frequency and $n_{2\omega} = 3.539$ at the second-harmonic frequency, and depth ranging from $d = 0.005\lambda$ to $d = 5.00\lambda$ in units of the fundamental wavelength in vacuum. The structure is assumed to be infinite and periodic in the $\hat{x}$ direction and infinite and uniform in the $\hat{y}$ direction. The nanostructure is illuminated by a normally incident plane wave at the fundamental frequency with wave vector $\vec{k}_{inc}$ and electric field $\vec{E}_{inc}$ polarized in the $\hat{y}$ direction.

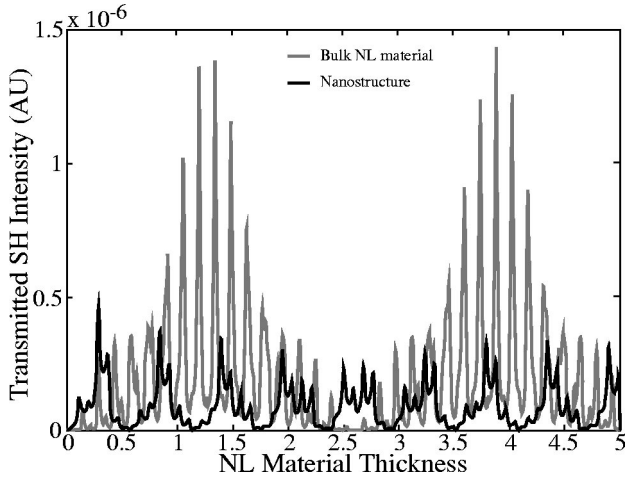

Fig. 2. Total transmitted SHG output intensity for the nanostructure shown in Fig. 1 and bulk nonlinear material as a function of depth.

Using the RCWA-based undepleted-pump SHG modeling tool, we investigate the total transmitted SHG output of the nanostructure and compare it with that of the bulk nonlinear material. Figure 2 shows the total transmitted SHG output of the structure as a function of depth for the nanostructure and the bulk material. For a certain range of depths, the nanostructure yields a greater SHG intensity output than the bulk material. The peak occurs for a depth of $d = 0.29\lambda$, with an output from the nanostructure approximately 2.05 times that of the bulk material of the same thickness. For greater material thicknesses, however, in most cases the nonlinear output of the bulk material exceeds that of the nanostructure. The oscillations in the total transmitted SHG intensity as a function of depth for both the nanostructure and the bulk material are due to Fabry–Perot effects and phase velocity mismatch between the fundamental and second-harmonic waves and will be considered in the following.

In order to analyze further the nonlinear output of the nanostructure, it is useful first to consider the results for the bulk nonlinear material shown in Fig. 2. It is clear that the transmitted SHG output as a function of

the nonlinear material thickness results from the superposition of several phenomena. First, the thin slab of nonlinear material acts as a Fabry–Perot cavity owing to the reflection from the front and back interfaces, thus modulating the output of the SHG process. For a given vacuum wavelength λ', the Fabry–Perot resonances are found at integer multiples of $l = \lambda'/(2n)$. The lowest-order resonant material thicknesses for the fundamental and second-harmonic frequencies are $l_\omega = 0.149\lambda$ and $l_{2\omega} = 0.071\lambda$, respectively. Although an approximation, it can be seen in Fig. 2 that the integer multiples of these two characteristic lengths correspond to the positions of the numerous narrow peaks in the total transmitted SHG of the bulk material. Second, we must also consider the phase mismatch between the fundamental and second-harmonic fields that is due to material dispersion. The effective propagation speeds of the fields inside the slab at the fundamental and second-harmonic frequencies are $v_\omega = 0.2989c$ and $v_{2\omega} = 0.2826c$, respectively (where c is the speed of light in vacuum), corresponding to a characteristic length of $l_c = 1.30\lambda$. Since this is the distance for the fundamental and second-harmonic fields to dephase by π, we expect the SHG output to reach a maximum at odd multiples of this characteristic length and to return to zero at even multiples of this length as a result of destructive interference. This corresponds to the envelope of the total transmitted SH intensity function for the bulk material case as seen in Fig. 2.

To understand the SHG output characteristics of the nanostructure, we will perform a similar analysis. However, we must first determine the propagation characteristics of the nanostructure modes. Using the RCWA method, we can obtain this information from the eigenvalues and eigenvectors of the periodic structure [see Eq. (A8)]. Each eigenvector describes one of the natural modes of the nanostructure, and the corresponding eigenvalue describes its propagation characteristics—the real part represents the decay coefficient, and the imaginary part represents the propagation constant (which is analogous to the wave vector for a plane wave). Furthermore, owing to the symmetry of the nanostructure with respect to the z axis (the finite dimension of the nanostructure), the eigenmodes will exist in pairs with eigenvalues of opposite sign, representing equivalent modes propagating in opposite directions. For clarity, in the following only one of each pair of eigenmodes is shown. Figure 3 shows results of an analysis of the nonevanescent energy-carrying modes of the nanostructure, obtained by selecting only those eigenmodes with a real part of the eigenvalue less than 10^{-8} in magnitude and an amplitude coefficient greater than 0.01 in magnitude. At the fundamental frequency there is only a single mode, shown in Fig. 3(a), which is transversely localized in the high-refractive-index region of the nanostructure, as predicted in our previous work.[8] In addition, there are two modes at the second-harmonic frequency, shown in Figs. 3(b) and 3(c), one localized in the high-refractive-index region and one localized primarily in the air gap of the nanostructure. Figure 3 also shows the real and imaginary parts of the eigenvalues for each of the modes. These constants correspond to Fabry–Perot resonance characteristic lengths of $l_\omega = 0.269\lambda$ for the fundamental mode and

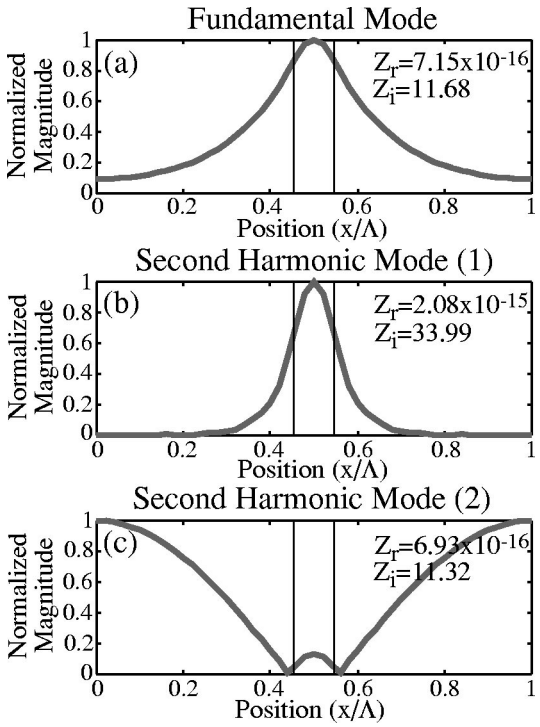

Fig. 3. Properties of the nonevanescent energy-carrying eigenmodes of the nanostructure shown in Fig. 1 for the (a) fundamental and (b), (c) second-harmonic wavelengths computed by using the modified RCWA tool: For each mode the transverse profile in one period of the nanostructure as well as the attenuation coefficient and propagation constant (real and imaginary parts of the corresponding eigenvalue Z respectively) are shown.

$l_{2\omega,1} = 0.278\lambda$ and $l_{2\omega,2} = 0.092\lambda$ for the second-harmonic modes. The phase velocities of the three modes shown in Figs. 3(a)–3(c) are $v_\omega = 0.538c$, $v_{2\omega,1} = 1.10c$, and $v_{2\omega,2} = 0.370c$, corresponding to phase matching characteristic lengths of $l_{c,1} = 0.527\lambda$ and $l_{c,2} = 0.592\lambda$. These parameters describe qualitatively the transmitted SHG intensity as a function of depth from the nanostructure.

For this nanostructure geometry, phase matching between the fundamental and either of the second-harmonic modes is not achieved for these depth ranges. Furthermore, since the difference in phase velocity is greater for the nanostructure than for the bulk material, we do not expect in general to be able to achieve enhanced SHG output from this nanostructure relative to the bulk material, despite the transverse field localization. In fact, the particular depths discussed above where the nanostructure yields a greater SHG transmitted intensity than the bulk material are due to the differing effective indices of refraction and the Fabry–Perot modes of the structure, resulting in a significantly higher fundamental field amplitude in the nanostructure in comparison with the bulk material of the same depth. However, the peak transmitted SH intensity from the nanostructure is approximately 30% of that obtained from the bulk material, although the nanostructure has only 9% of the nonlinear material by volume as well as a greater phase mismatch between the fundamental and SH fields. This fact suggests that the nanostructure does in fact contribute to the enhancement of the SHG process through transverse localization of the

field; but to achieve superior performance, phase matching must be realized in the nanostructure.

B. Phase Matching

To implement a SHG enhancement nanostructure that incorporates both transverse field localization and phase matching, we investigate an alternative nanostructure having two ridges per period, instead of one. In Subsection 3.A we found that the fundamental frequency mode of the nanostructure is transversely localized in the high-refractive-index region, while the second-harmonic frequency mode of interest is transversely localized in the low-refractive-index region and has a phase velocity significantly higher than that of the fundamental frequency mode. Thus we expect that the introduction of a second, smaller nonlinear material ridge into the center of the low-refractive-index region will affect the phase velocity of the second-harmonic mode more dramatically. Specifically, the introduction of a high-refractive-index material in a region where the fundamental mode has a low amplitude but the second-harmonic mode has a large amplitude will serve to significantly reduce the phase velocity of the second harmonic mode while leaving the fundamental mode largely unaffected. By engineering this differential slowing of the two modes to exactly compensate for the existing phase velocity mismatch between the two modes, we can achieve phase matching. It is important to point out that the second material ridge must be smaller than the original nanostructure ridge; otherwise, the mode properties of the nanostructure would be qualitatively changed. As in the previous example, for clarity we consider a nanostructure that is infinitely periodic in the $\hat{x}$ direction, infinite and uniform in the $\hat{y}$ direction, finite, uniform in the $\hat{z}$-direction, surrounded by vacuum on both sides, and not explicitly including the substrate.

A schematic drawing of the structure is shown in Fig. 4. The period of the grating is again $\Lambda = 0.65\lambda$, and the fill

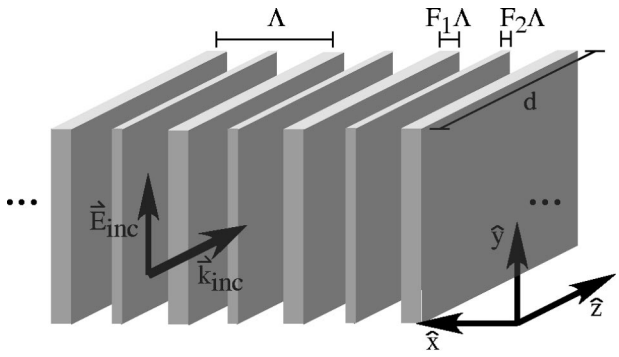

Fig. 4. Schematic diagram of the modified transverse field localization nanostructure with improved phase matching, consisting of a periodic subwavelength grating having two nonlinear material ridges with fill factors $F_1 = 0.063$ and $F_2 = 0.03$ per period $\Lambda = 0.65\lambda$. The index of refraction is $n_\omega = 3.346$ at the fundamental frequency and $n_{2\omega} = 3.539$ at the second-harmonic frequency, and the depth ranges from $d = 0.005\lambda$ to $d = 5.00\lambda$ in units of the fundamental wavelength in vacuum. The structure is assumed to be infinite and periodic in the $\hat{x}$ direction and infinite and uniform in the $\hat{y}$ direction. The nanostructure is illuminated by a normally incident plane wave at the fundamental frequency with wave vector $\vec{k}_{\text{inc}}$ and electric field $\vec{E}_{\text{inc}}$ polarized in the $\hat{y}$ direction.

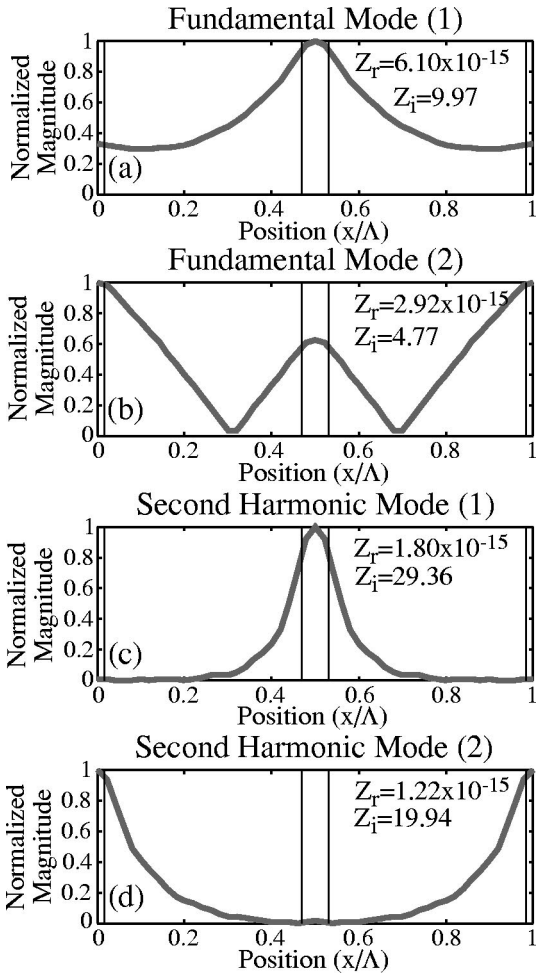

Fig. 5. Properties of the nonevanescent energy-carrying eigenmodes of the modified nanostructure shown in Fig. 4 for the (a), (b) fundamental and (c), (d) second-harmonic wavelengths computed by using the modified RCWA tool: For each mode the transverse profile in one period of the nanostructure as well as the attenuation coefficient and propagation constant (real and imaginary parts of the corresponding eigenvalue Z) are shown.

factors of the two ridges are $F_1 = 0.063$ and $F_2 = 0.03$. Analyzing the nonevanescent energy-carrying modes of the nanostructure, we find two modes each at the fundamental and second-harmonic frequencies, which are shown in Figs. 5(a)–5(d). At each frequency, one mode is localized in the wide nonlinear material ridge (with fill factor F_1) shown in the center of the figure, while the other mode is localized primarily in the narrow second ridge (with fill factor F_2). Figure 5 also shows the real and imaginary parts of the mode propagation constants of the four modes.

To verify the ability to control the phase velocities of the fundamental and second-harmonic modes by using the geometry of the nanostructure, we investigate the dependence of the mode phase velocities on the fill factors F_1 and F_2 of the nanostructure. We compute the phase velocities of the four modes as a function of the narrow-ridge fill factor F_2 while keeping the wide-ridge fill factor $F_1 = 0.063$ constant, as shown in Fig. 6. In this case, the fundamental and second-harmonic modes that are localized in the wide F_1 ridge [labeled F-1 and SH-1 in Fig. 6, corresponding to the modes shown in Figs. 5(a) and 5(c),

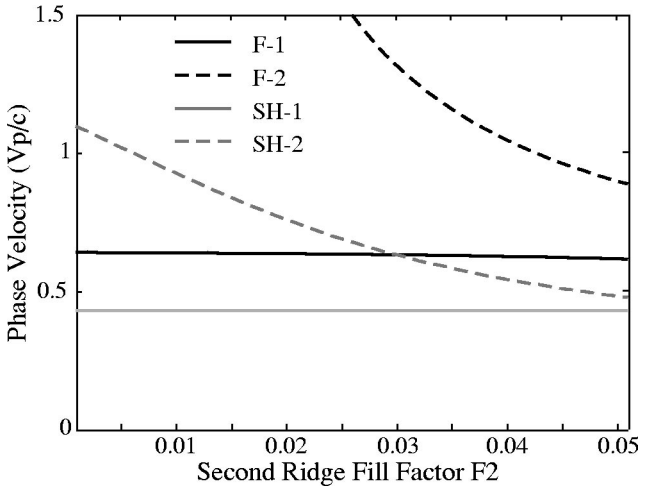

Fig. 6. Phase velocities of the two fundamental (F-1 and F-2) and two second-harmonic (SH-1 and SH-2) nonevanescent energy-carrying eigenmodes of the nanostructure shown in Fig. 4 as a function of fill factor F_2 with $F_1 = 0.063$ constant.

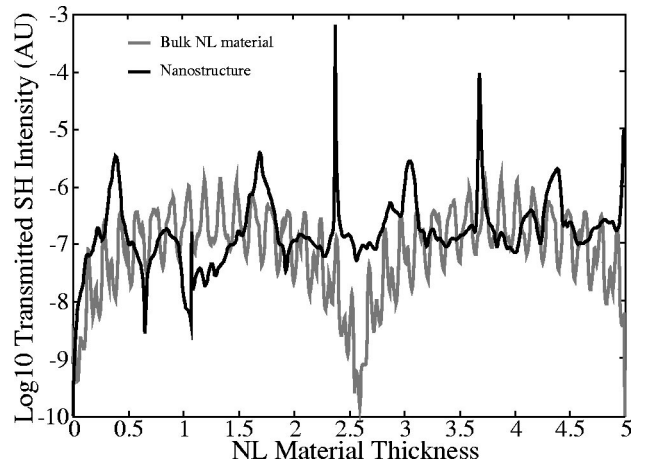

Fig. 7. Total transmitted SHG output intensity for the modified nanostructure shown in Fig. 4 and bulk nonlinear material as a function of depth.

respectively] have an approximately constant phase velocity with respect to F_2, while the other two modes [labeled F-2 and SH-2 in Fig. 6, corresponding to the modes shown in Figs. 5(b) and 5(d), respectively] exhibit a dependence of their phase velocity on the parameter F_2. Thus the phase velocities of the fundamental mode localized in the wide F_1 ridge and the second-harmonic mode localized in the narrow F_2 ridge can be adjusted essentially independently through the geometry of the nanostructure. More important, the phase velocities can be made equal to achieve phase matching for SHG, as shown in Fig. 6, for the nanostructure geometry shown in Fig. 4.

Using the mode propagation constants from Figs. 5(a), 5(b), 5(c), and 5(d) for the geometry shown in Fig. 4, we find the phase velocities of the modes to be $v_{\omega,1} = 0.630c$, $v_{\omega,2} = 1.32c$, $v_{2\omega,1} = 0.428c$, and $v_{2\omega,2} = 0.630c$, respectively. The addition of the second high-refractive-index ridge results in good matching of the phase velocities of the "slow" fundamental frequency mode ($v_{\omega,1}$) and the "fast" second-harmonic frequency mode ($v_{2\omega,2}$). The characteristic length of the propagation constant mismatch of these two modes is $l_c = 981.8\lambda$. As a result, we expect that phase mismatch will not significantly affect the output of the nonlinear process in the modified nanostructure, at least over the practical nanostructure sizes under consideration. Phase matching in the modified nanostructure results in a significant enhancement of the second-harmonic output relative to the original nanostructure design as well as to the bulk nonlinear material.

A comparison of the total transmitted SHG intensity of the modified nanostructure and bulk material as a function of the nonlinear material depth is shown in Fig. 7. For both the nanostructure and the bulk material, Fabry–Perot effects still strongly affect the SHG output. However, maxima of the total transmitted SHG output of the nanostructure are significantly higher than those of the bulk material. For example, for a depth $d = 0.395\lambda$, the nanostructure yields a total transmitted SHG intensity of approximately 2.4 times the maximum obtained from the phase-mismatched bulk material for any depth shown; and for a depth $d = 2.382\lambda$, the ratio is approximately 463. As shown in Fig. 7, the peak corresponding to the enhanced SHG output in the latter case is extremely narrow, suggesting that the elevated output is strongly dependent on the longitudinal resonances of the nanostructure. In contrast, in the former case the width of the enhanced SHG output peak is relatively broad, suggesting that the lower enhancement factor can be achieved without extreme sensitivity to the nanostructure geometry (thus requiring less rigid fabrication tolerances). In addition, in the former case the structure depth is significantly less than the characteristic phase matching length in the bulk material, indicating that the elevated SHG output of the modified nanostructure is not solely the result of longitudinal resonances or improved phase matching in the nanostructure. Furthermore, the fact that the modified nanostructure consists of only 9.3% nonlinear material by volume emphasizes the importance of the transverse near-field localization effect in the nanostructure. Thus these results demonstrate that subwavelength periodic optical nanostructures can be applied to enhance SHG via two mechanisms: (1) transverse field localization in the nonlinear material to increase the peak power and (2) engineering of the propagation speeds of the fundamental and SH modes to achieve phase matching.

4. CONCLUSION

We have extended the well-established RCWA algorithm to analyze SHG in periodic nanostructures in the undepleted-pump approximation. This nonlinear electromagnetic modeling tool permits rigorous analysis of the structure and propagation characteristics of the nanostructure modes, facilitating the investigation of near-field phenomena in the nanostructures as well as the design of novel nonlinear optical devices. In principle, it would be possible to continue the perturbation expansion of the nonlinear polarization term, permitting the analysis of downconversion (including the depleted-pump case) as well as other nonlinear optical phenomena of interest, but much more computational power would be required.

In addition, using this tool, we have investigated two nanostructures for enhanced SHG. In the first case, a structure for transverse localization of the field in the nonlinear material provides evidence of enhanced performance resulting from the field localization, but the overall transmitted SHG output of the device was lower than that of the bulk material owing to phase mismatch in the structure. In the second case, the nanostructure was modified to achieve phase matching through the introduction of a second high-refractive-index material ridge per period. This structure yields increased SHG transmitted intensity in comparison with the bulk nonlinear material, more than two orders of magnitude in some cases, despite the fact that it is composed of only 9.3% nonlinear material by volume. Thus, using the additional design degrees of freedom provided by the periodic nanostructure makes it possible to construct a device capable of enhancing SHG efficiency through both transverse near-field localization and phase matching in an isotropic nonlinear material. As a result, this approach could provide significantly improved performance in comparison with other microstructure- and nanostructure-based techniques to enhance SHG efficiency, albeit by using a more complex nanostructure with smaller features. The relative merits of the various optical nonlinearity enhancement techniques depend strongly on the nature and requirements of the specific application of interest; thus a direct comparative analysis is beyond the scope of this paper and will be investigated in the future.

Finally, the presence of significant Fabry–Perot effects indicates that longitudinal localization of the field in the cavity formed by the nanostructure is present and dramatically influences the SHG output. In fact, the application of the longitudinal modes of resonant cavities to enhance the field amplitude and thus nonlinear optical effects is a well-known technique. More-advanced device designs could eliminate cavity effects through nanostructured antireflection layers to relax design tolerances or to take advantage of cavity phenomena by using photonic crystal techniques to further enhance the nonlinear output. Finally, an important benefit of this approach to enhance the efficiency of SHG in nanostructures is that the materials and designs used are compatible with standard microfabrication techniques, facilitating integration with other photonic devices and systems.

APPENDIX A: SUMMARY OF STANDARD RIGOROUS COUPLED-WAVE ANALYSIS FORMULATION

This appendix, included for completeness, summarizes the standard formulation of RCWA and introduces the notation used in this paper. A more detailed description of the method can be found in Refs. 20–24. The grating region is taken to be infinitely periodic in one transverse dimension (x) with grating period Λ, infinite and uniform in the other transverse dimension (y), and finite and uniform in the depth dimension (z). The dielectric constant function inside the grating may be a tensor to account for anisotropic materials, but it depends only on the coordinate x and is a periodic function:

$$\bar{\epsilon}(\vec{r}) = \bar{\epsilon}(\vec{r} + \Lambda\hat{x}) = \begin{cases} \bar{\epsilon}_\omega(x), & 0 < z < d \\ \epsilon_0 & z < 0; z > d \end{cases}. \tag{A1}$$

The incident field is assumed to be a monochromatic plane wave of unit amplitude with wave vector $\vec{k}_{\text{inc}}$. Under these assumptions, the electric and magnetic fields inside the grating region may be represented by using a space-harmonic field expansion:

$$\vec{E}_\omega(\vec{r}) = \sum_i \{S_{\omega,i,x}(z)\hat{x} + S_{\omega,i,y}(z)\hat{y} + S_{\omega,i,z}(z)\hat{z}\}\exp(-j\vec{\sigma}_{\omega,i}\cdot\vec{r}), \tag{A2}$$

$$\vec{H}_\omega(\vec{r}, t) = \sqrt{\frac{\epsilon_0}{\mu_0}}\sum_i [U_{\omega,i,x}(z)\hat{x} + U_{\omega,i,y}(z)\hat{y} + U_{\omega,i,z}(z)\hat{z}]\exp(-j\vec{\sigma}_{\omega,i}\cdot\vec{r}), \tag{A3}$$

where $\vec{S}_{\omega,i}$ and $\vec{U}_{\omega,i}$ are the space-harmonic-expansion amplitude coefficients for the electric and magnetic fields, respectively, ϵ_0 is the dielectric permittivity of free space, and μ_0 is the magnetic permeability of free space. The space-harmonic expansion contains a total of $p = 2a + 1$ elements, referenced by index $i \in \{-a, \ldots, -1, 0, 1, \ldots, a\}$. The transverse component of the wave vector is given by

$$\vec{\sigma}_{\omega,i} = (k_{\text{inc},x} - iK_g)\hat{x} + k_{\text{inc},y}\hat{y}, \tag{A4}$$

where $K_g = 2\pi/\Lambda$. Since the grating is periodic, the (vw) component ($v, w \in \{x, y, z\}$) of the dielectric constant tensor can also be expanded in a space-harmonic series:

$$\epsilon_{\omega,vw}(x) = \epsilon_0\sum_k \tilde{\epsilon}_{\omega,k,vw}\exp(jkK_g x). \tag{A5}$$

A similar expansion is performed for the electric and magnetic fields in the half-spaces on either side of the grating region. Inserting Eqs. (A2), (A3), and (A5) into Maxwell's equations and simplifying produces a coupled system of first-order partial differential equations:

$$\frac{\partial}{\partial z}\begin{pmatrix} \vec{S}_{\omega,x}(z) \\ \vec{S}_{\omega,y}(z) \\ \vec{U}_{\omega,x}(z) \\ \vec{U}_{\omega,y}(z) \end{pmatrix} = \mathbf{A}_\omega\begin{pmatrix} \vec{S}_{\omega,x}(z) \\ \vec{S}_{\omega,y}(z) \\ \vec{U}_{\omega,x}(z) \\ \vec{U}_{\omega,y}(z) \end{pmatrix}, \tag{A6}$$

where the matrix $\mathbf{A}_\omega$ is determined by the structure of the grating and Maxwell's equations [see, for example, Eq. (32) of Ref. 24 for a detailed description], and the vector $\vec{S}_{\omega,x}(z)$ contains the $p = 2a + 1$ elements of the space-harmonic expansion coefficients

$$\vec{S}_{\omega,x}(z) = \begin{pmatrix} \vec{S}_{\omega,-a}(z) \\ \vec{S}_{\omega,-a+1}(z) \\ \cdots \\ \vec{S}_{\omega,a}(z) \end{pmatrix}, \tag{A7}$$

with a similar expansion for the vectors $\vec{S}_{\omega,y}(z)$, $\vec{U}_{\omega,x}(z)$, and $\vec{U}_{\omega,y}(z)$.

Using the eigenvector matrix $\mathbf{W}_\omega$ corresponding to the matrix $\mathbf{A}_\omega$, we can write the solution to Eq. (A6) as

$$\begin{pmatrix} \vec{S}_{\omega,x}(z) \\ \vec{S}_{\omega,y}(z) \\ \vec{U}_{\omega,x}(z) \\ \vec{U}_{\omega,y}(z) \end{pmatrix} = \mathbf{W}_\omega \exp(\mathbf{D}z)\vec{c}_\omega, \tag{A8}$$

where $\vec{c}_\omega$ is a vector of length $4p$ containing the amplitude coefficients of each eigenmode and the matrix $\mathbf{D}$ is a diagonal matrix containing the eigenvalues. Using Eq. (A8) to propagate the fields across the grating region, and applying the appropriate boundary conditions at each interface, we can find the amplitude coefficients $\vec{c}_\omega$ (see, for example, Ref. 20 for a more detailed explanation).

ACKNOWLEDGMENTS

This work is supported in part by the National Science Foundation, the Defense Advanced Research Projects Agency, and the U.S. Air Force Office of Scientific Research.

Corresponding author Wataru Nakagawa is at the Department of Electrical and Computer Engineering, University of California, San Diego, 9500 Gilman Drive, La Jolla, California, 92093-0407; phone, 858-534-7208; e-mail, wnakagaw@ucsd.edu.

REFERENCES

1. P. Lalanne and J.-P. Hugonin, "High-order effective-medium theory of subwavelength gratings in classical mounting: application to volume holograms," J. Opt. Soc. Am. A **15**, 1843–1851 (1998).
2. J. N. Mait, D. W. Prather, and M. S. Mirotznik, "Design of binary subwavelength diffractive lenses by use of zeroth-order effective-medium theory," J. Opt. Soc. Am. A **16**, 1157–1167 (1999).
3. F. Xu, R.-C. Tyan, P.-C. Sun, Y. Fainman, C.-C. Cheng, and A. Scherer, "Form-birefringent computer-generated holograms," Opt. Lett. **21**, 1513–1515 (1996).
4. R.-C. Tyan, A. A. Salvekar, H.-P. Chou, C.-C. Cheng, A. Scherer, P.-C. Sun, F. Xu, and Y. Fainman, "Design, fabrication and characterization of form-birefringent multilayer polarizing beam splitter," J. Opt. Soc. Am. A **14**, 1627–1636 (1997).
5. E. Yablonovitch, "Photonic band-gap structures," J. Opt. Soc. Am. B **10**, 283–295 (1993).
6. R.-C. Tyan, P.-C. Sun, A. A. Salvekar, H.-P. Chou, C.-C. Cheng, F. Xu, A. Scherer, and Y. Fainman, "Subwavelength multilayer binary grating design for implementing photonic crystals," in *Quantum Optoelectronics*, Vol. 9 of 1997 OSA Technical Digest Series (Optical Society of America, Washington D.C., 1997), pp. 35–37.
7. W. Nakagawa, P.-C. Sun, C.-H. Chen, and Y. Fainman, "Wide-field-of-view narrow-band spectral filters based on photonic crystal nanocavities," Opt. Lett. **27**, 191–193 (2002).
8. W. Nakagawa, R.-C. Tyan, P.-C. Sun, and Y. Fainman, "Near-field localization of ultrashort optical pulses in transverse 1-D periodic nanostructures," Opt. Express **7**, 123–128 (2000), http://www.opticsexpress.org.
9. J. E. Sipe and R. W. Boyd, "Nonlinear susceptibility of composite optical materials in the Maxwell Garnett model," Phys. Rev. A **46**, 1614–1629 (1992).
10. R. W. Boyd and J. E. Sipe, "Nonlinear optical susceptibilities of layered composite materials," J. Opt. Soc. Am. B **11**, 297–303 (1994).
11. G. L. Fischer, R. W. Boyd, R. J. Gehr, S. A. Jenekhe, J. A. Osaheni, J. E. Sipe, and L. A. Weller-Brophy, "Enhanced nonlinear optical response of composite materials," Phys. Rev. Lett. **74**, 1871–1874 (1995).
12. K. P. Yuen, M. F. Law, K. W. Yu, and P. Sheng, "Enhancement of optical nonlinearity through anisotropic microstructures," Opt. Commun. **148**, 197–207 (1998).
13. H. Ma, R. Xiao, and P. Sheng, "Third-order optical nonlinearity enhancement through composite microstructures," J. Opt. Soc. Am. B **15**, 1022–1029 (1998).
14. A. Fiore, S. Janz, L. Delobel, P. van der Meer, P. Bravetti, V. Berger, E. Rosencher, and J. Nagle, "Second-harmonic generation at $\lambda = 1.6\ \mu$m in AlGaAs/Al_2O_3 waveguides using birefringence phase matching," Appl. Phys. Lett. **72**, 2942–2944 (1998).
15. A. Fiore, V. Berger, E. Rosencher, P. Bravetti, and J. Nagle, "Phase matching using an isotropic nonlinear optical material," Nature (London) **391**, 463–466 (1998).
16. A. Saher Helmy, D. C. Hutchings, T. C. Kleckner, J. H. Marsh, A. C. Bryce, J. M. Arnold, C. R. Stanley, J. S. Aitchison, C. T. A. Brown, K. Moutzouris, and M. Ebrahimzadeh, "Quasi phase matching in GaAs-AlAs superlattice waveguides through bandgap tuning by use of quantum-well intermixing," Opt. Lett. **25**, 1370–1372 (2000).
17. L. A. Eyres, P. J. Tourreau, T. J. Pinguet, C. B. Ebert, J. S. Harris, M. M. Fejer, L. Becouarn, B. Gerard, and E. Lallier, "All-epitaxial fabrication of thick, orientation-patterned GaAs films for nonlinear optical frequency conversion," Appl. Phys. Lett. **79**, 904–906 (2001).
18. K. Moutzouris, S. Venugopal Rao, M. Ebrahimzadeh, A. De Rossi, V. Berger, M. Calligaro, and V. Ortiz, "Efficient second-harmonic generation in birefringently phase-matched GaAs/Al_2O_3 waveguides," Opt. Lett. **26**, 1785–1787 (2001).
19. E. U. Rafailov, P. Loza-Alvarez, C. T. A. Brown, W. Sibbett, R. M. De La Rue, P. Millar, D. A. Yanson, J. S. Roberts, and P. A. Houston, "Second-harmonic generation from a first-order quasi-phase-matched GaAs/AlGaAs waveguide crystal," Opt. Lett. **26**, 1984–1986 (2001).
20. M. G. Moharam and T. K. Gaylord, "Diffraction analysis of dielectric surface-relief gratings," J. Opt. Soc. Am. **72**, 1385–1392 (1982).
21. M. G. Moharam, E. B. Grann, D. A. Pommet, and T. K. Gaylord, "Formulation for stable and efficient implementation of the rigorous coupled-wave analysis of binary gratings," J. Opt. Soc. Am. A **12**, 1068–1076 (1995).
22. E. N. Glytsis and T. K. Gaylord, "Rigorous three-dimensional coupled-wave diffraction analysis of single and cascaded anisotropic gratings," J. Opt. Soc. Am. A **4**, 2061–2080 (1987).
23. L. Li, "Use of Fourier series in the analysis of discontinuous periodic structures," J. Opt. Soc. Am. A **13**, 1870–1876 (1996).
24. L. Li, "Reformulation of the Fourier modal method for surface-relief gratings made with anisotropic materials," J. Mod. Opt. **45**, 1313–1334 (1998).